Check for updates

The emergence of a robust lithium gallium oxide surface layer on gallium-doped LiNiO$_2$ cathodes enables extended cycling stability†

Mritunjay Mishra [ID] [b] and Koffi P. C. Yao [ID] *[a]

LiNiO$_2$ is a promising cobalt-free cathode for lithium-ion batteries due to its high theoretical capacity and low cost. Although intensely studied, the occurrence of several phase transformations and particle pulverization causing capacity fading in cobalt-free LiNiO$_2$ have yet to be effectively resolved. Herein, a sol−gel synthesis process is utilized for gallium (Ga) doping of LiNiO$_2$ at 2% (solution-doping) and 5% (excess-doping) molar ratios. Transmission electron microscopy and X-ray diffraction Rietveld refinement reveal the opportune formation of an α-LiGaO$_2$ shell at 5% doping beyond the solubility limit of 2%. Alongside solution-doping at the Ni and Li crystallographic sites, the emergence of this α-LiGaO$_2$, isostructural and lattice-matched to the $R\bar{3}m$ LiNiO$_2$, is shown to improve capacity retention by a factor of 2.45 after 100 cycles at C/3. Particles with the LiGaO$_2$ shell experience significantly less pulverization during extended cycling. In contrast, the solution-doped LiNiO$_2$ with 2% Ga experiences extensive particle fracturing similar to the baseline undoped LiNiO$_2$. In turn, no significant electrochemical performance difference is found between the solution-doped and baseline LiNiO$_2$. The evidence garnered suggests that a surface gallium oxide phase achievable with excess Ga is key to enabling extended cycling using Ga doping.

Introduction

The surge in demand for energy storage has prompted the search for lower-cost lithium-ion battery materials. To ease supply bottlenecks and thereby lower cost, batteries free of contentious cobalt are intensely desired by industries and governments. Among several compositions of cathodes the scientific community hopes to expand the family of viable transition metal oxides LiMO$_y$ (where M = Mn, Ni, Fe...) due to their inherent ability to seamlessly intercalate and deintercalate lithium within layered structures.[1,2] LiNiO$_2$ in particular can achieve theoretical capacities upward of 270 mA h g^{-1} with the participation of one mole of lithium in the intercalation process.[3] Furthermore, LiNiO$_2$ would be a cobalt-free alternative to LiNi$_x$Mn$_y$Co$_z$O$_2$ (NMC) high-capacity chemistries in use today. Despite the numerous advantages of cobalt-free LiNiO$_2$ such as its high energy density, favorable redox properties

(Ni^{3+} → Ni^{4+} conversion largely achievable from 3.0 to 4.3 V), and drop-in compatibility with existing cobalt-bearing chemistries, there are several challenges that hinder its commercialization. The H$_2$ ↔ H$_3$ phase transformation appears detrimental to sustained cycling.[4] Repeated transitions with the accompanying fluctuations in unit cell volume result in fatigue strain within the material. The aforementioned stresses induce deformation and microstructural damage to the particles. Particle cracking increases the electrochemical surface area and electrolyte penetration, which promotes excessive formation of cathode-electrolyte interphases (CEI). The interphase growth consumes electrolyte and Li$^+$ inventory, thereby compromises long-term cycling stability.[5,6] At deeper charge-states, transition from an O3-type (ABCABC stacking) to an O1-type (ABAB) lattice due to interlayer anionic repulsion at low lithium contents occurs, which exacerbates the mechanical instability.[4]

Another major challenge facing the viability of LiNiO$_2$ is the pervasive oxygen (O$_2$) loss at high potential yielding detrimental spinel and rock-salt surface phases. Biasi *et al.*[7] utilized operando X-ray diffraction (XRD) and differential electrochemical mass spectrometry (DEMS) to gain insight into the dynamics impacting the stability of LiNiO$_2$. The authors reported vigorous O$_2$ evolution in the solid-solution regions of H$_2$ and H$_3$ phases, which dropped to a local minimum during the actual H$_2$ ↔ H$_3$ transformation. In contrast, DEMS by Park *et al.*[8]

[a] Department of Mechanical Engineering, University of Delaware, Newark, Delaware 19716, USA. E-mail: claver@udel.edu

[b] Department of Chemistry and Biochemistry, University of Delaware, Newark, Delaware 19716, USA

† Electronic supplementary information (ESI) available: Variance and SD calculations, literature review, XRD fittings and refinement results, EDS (line scan) data and line scan simulation, impedance profile, differential capacity plot, and SEM images of cycled electrodes. See DOI: **https://doi.org/10.1039/d3ma01102j**

found O_2 loss on uncoated-$LiNiO_2$ spanning the entire $H_2 \leftrightarrow H_3$ transformation range while minimal O_2 loss from graphene-coated $LiNiO_2$ coincides with a depressed $H_2 \rightarrow H_3$ peak and extended cycling. Hu *et al.*[9] quantified the gas evolution by single crystal and polycrystalline nickel-rich $LiNi_{0.76}Mn_{0.14}Co_{0.1}O_2$ (NMC76) using DEMS. They observed the onset of O_2 evolution at 4.5 V on polycrystalline NMC76. Undetectable O_2 evolution in the single crystal counterparts coincided with extended cycling stability of the nickel-rich oxide. Wang *et al.*[10] used *in situ* XRD to correlate the mechanical breakdown of $LiNiO_2$ and Mg/Ti-doped $LiNiO_2$ cathodes with O_2 loss during charge–discharge cycling. The authors *in situ* electron microscopy show the emergence of stacking faults identified as O1 from O_2 loss induced by elevated temperatures and supported by *ab initio* molecular dynamic (MD) calculations. The authors also resolved *via* electron tomography the emergence of cracks both in the bulk and on the surface of particles upon the O_2 release. Cheng *et al.*[11] used DFT to estimate the average O_2 release energy from $LiNiO_2$ at various lithiation states. From fully lithiated $Li_{1-x}NiO_2$ ($x = 0$) to 75% delithiated $Li_{1-x}NiO_2$ ($x = 0.75$), the O_2 release energy drops from 1.27 eV to 0.15 eV at $T = 30\ ^{\circ}C$ and $p(O_2) = 0.2$ atm. External energy input such as an increase in the temperature to $T = 200\ ^{\circ}C$ is predicted to result in a spontaneous O_2 loss in $Li_{1-x}NiO_2$ ($x = 0.75$) with a release energy of -0.05 eV. This finding is thermodynamically consistent with the fact that O_2 release is ubiquitous under a high applied potential (> 4.0 V *vs.* Li/Li^+) as per the experimental gas analysis studies listed above.

From the preponderance of evidence in the literature, O_2 release with the accompanying mechanical damage and irreversible phase conversion appears incontrovertible for the neat (polycrystalline) $LiNiO_2$. However, Cheng *et al.*[11] predicted that the addition of dopants with an affinity for surface segregation would increase the average O_2 release energy in 75% delithiated $Li_{1-x}NiO_2$. Dopants such as tungsten (W), antimony (Sb),

tantalum (Ta), and titanium (Ti) increase the predicted O_2 release energy to 0.53, 0.56, 0.40 and 0.35 eV, respectively. Synthesized 2% Sb doped $LiNiO_2$ with the most positive O_2 release energy retains $\sim 5\%$ higher capacity compared to undoped $LiNiO_2$ at C/5 over 60 cycles.

As it stands, a variety of dopants shown in Table S1 (ESI†) have been explored to stabilize the cycling of $LiNiO_2$ including multi-atomic dopants. Fig. 1 summarizes data collected for dopants gallium (Ga), tungsten (W), niobium (Nb), aluminum (Al), and zirconium (Zr). A notable feature is the variability of capacity retention of undoped $LiNiO_2$ prepared by various research groups using different synthesis approaches. The calculated variances for all dopants recorded in Fig. 1 are provided in Table S2 (ESI†). A standard deviation $\sigma \approx 20\%$ is calculated for undoped $LiNiO_2$ from the 50th cycle data collected herein.[12–27] The data collected for Al, Nb, Zr, and W show less prominent variance, albeit possibly due to a concentration of publications in a small set of laboratories; the obtained standard deviations are below 10%. Ga in $LiNiO_2$ has a binding affinity for oxygen and may improve structural stability during cycling. Wu *et al.*[13] found that introducing Ga at the manganese (Mn) site in nickel-rich layered oxide cathode materials (NCM) effectively mitigates cation mixing at synthesis, which boosts capacity retention and thermal stability. Ga as a dopant holds promise towards increasing the longevity of $LiNiO_2$;[14,16,17] nonetheless, capacity retention data over 50 cycles show a variance ($\sigma \approx 17\%$) similar to that of undoped $LiNiO_2$. For example, Nishida *et al.*[17] demonstrated nearly 100% capacity retention after 50 cycles for 2% Ga-doped $LiNiO_2$ while Song *et al.*[22] reported $\sim 45\%$ retention after the same 50 cycles with 2.5% Ga-doped $LiNiO_2$. The high variance is due to a significant part of Ga incorporating into the bulk (solid-solution) as well as segregating as lithiated gallium oxide secondary phases, the function of the latter still being largely unclear. From XRD analysis, Kitsche *et al.*[14] reported that the introduction of 2–5%
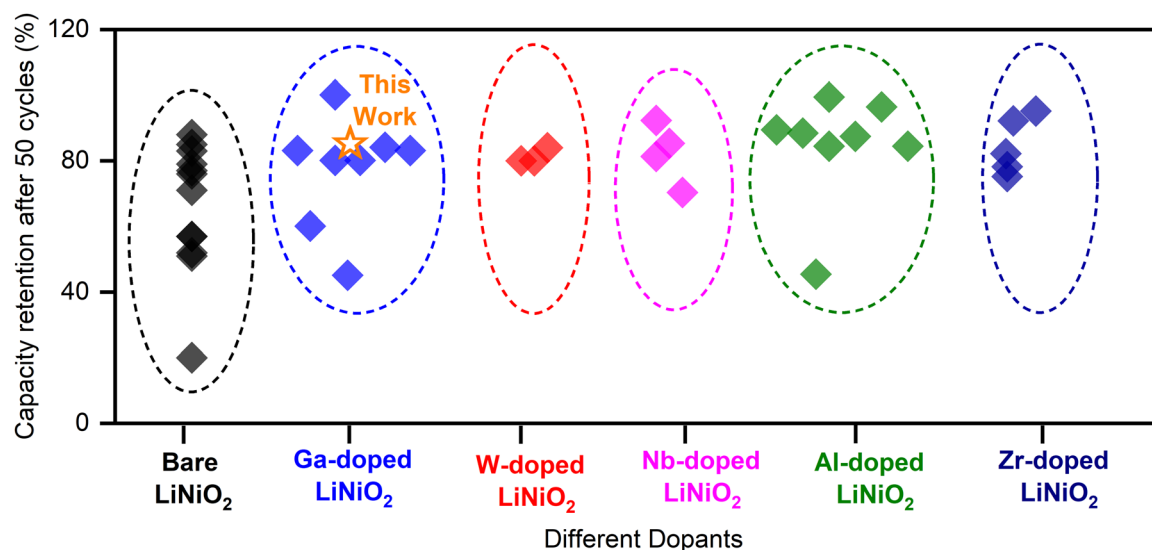

Fig. 1 Capacity retention at 50 cycles for $LiNiO_2$ with various dopants from the literature.[12–27]

nominal Ga mole fraction, which exceeds the solubility limit estimated at 2%, lead to the formation of the Li_5GaO_4 impurities. From 2% up to 5% nominal Ga doping, the capacity retention of $Li_{1-y}Ga_yNiO_2$ after 100 cycles at C/2 jumped from ~ 80 mA h g^{-1} to 140–150 mA h g^{-1}. The best performance is achieved at 4% Ga which retained 78% of its initial capacity after 100 C/2 charge–discharge cycles. The report is not definitive as to whether the improved retention stems from a positive impact of the Li_5GaO_4 impurities (possibly a surface coating) or from the bulk doping of Ga within the $LiNiO_2$ lattice. The uncertainty as to the origin of measurable improvements with Ga doping prompts the present contribution. It is hypothesized here that surface gallium oxide is key to stabilizing the electrochemical cycling under Ga doping.

Herein, a comparison is made between undoped, solution-doped (near solubility of 2% Ga), and excess-doped $LiNiO_2$ (5% Ga) in an effort to discern the role of secondary gallium oxide phases. Our sol–gel synthesis in the presence of excess Ga resulted in an unexpected (reported single-phase synthesis at 3 MPa synthesis pressure[28]) lithium gallate (α-$LiGaO_2$) phase on the surface of the $LiNiO_2$ particles. The α-$LiGaO_2$ (symmetry: $R\bar{3}m$, lattice: $a = b \approx 2.911$ Å, $c \approx 14.466$ Å) surface phase may have formed at the standard synthesis pressure because of its lattice-match against $LiNiO_2$ (symmetry: $R\bar{3}m$, lattice: $a = b \approx 2.8713$ Å, $c \approx 14.1861$ Å). The formation enthalpy of

$LiGaO_2$ ($\Delta H_f = -918.352$ kJ mole^{-1}) is $\sim 50\%$ more exothermic than that of $LiNiO_2$ ($\Delta H_f = -612.450$ kJ mole^{-1}) forecasting a greater thermodynamic barrier to O_2 loss from $LiGaO_2$ as a surface phase on $LiNiO_2$. The simultaneous surface coating and solution-doping of the $LiNiO_2$ enhanced the capacity retention by a factor of 2.45 over the undoped $LiNiO_2$. In contrast, the solution-doped $LiNiO_2$ yielded no measurable boost in capacity retention. Post-cycling scanning electron microscopy (SEM) indicates that the excess-doped $LiNiO_2$ withstands pulverization after 100 cycles while the solution-doped and undoped $LiNiO_2$ fracture extensively. These findings suggest that the $LiGaO_2$ surface layer is key to preserving the structural and surface integrity of the material towards extended cycling. The findings offer an informed approach to enhancing the electrochemical performance of cobalt-free $LiNiO_2$ with Ga doping.

Experimental

Synthesis

In nominal molar ratio terms, 1% Ga-doped $LiNiO_2$ (denoted "1% Ga–$LiNiO_2$") to 6% Ga-doped $LiNiO_2$ (denoted "6% Ga–$LiNiO_2$") were synthesized for comparison with the baseline $LiNiO_2$. A sol–gel synthesis route was utilized as illustrated in Scheme 1. To produce $LiNiO_2$ powders doped with different Ga
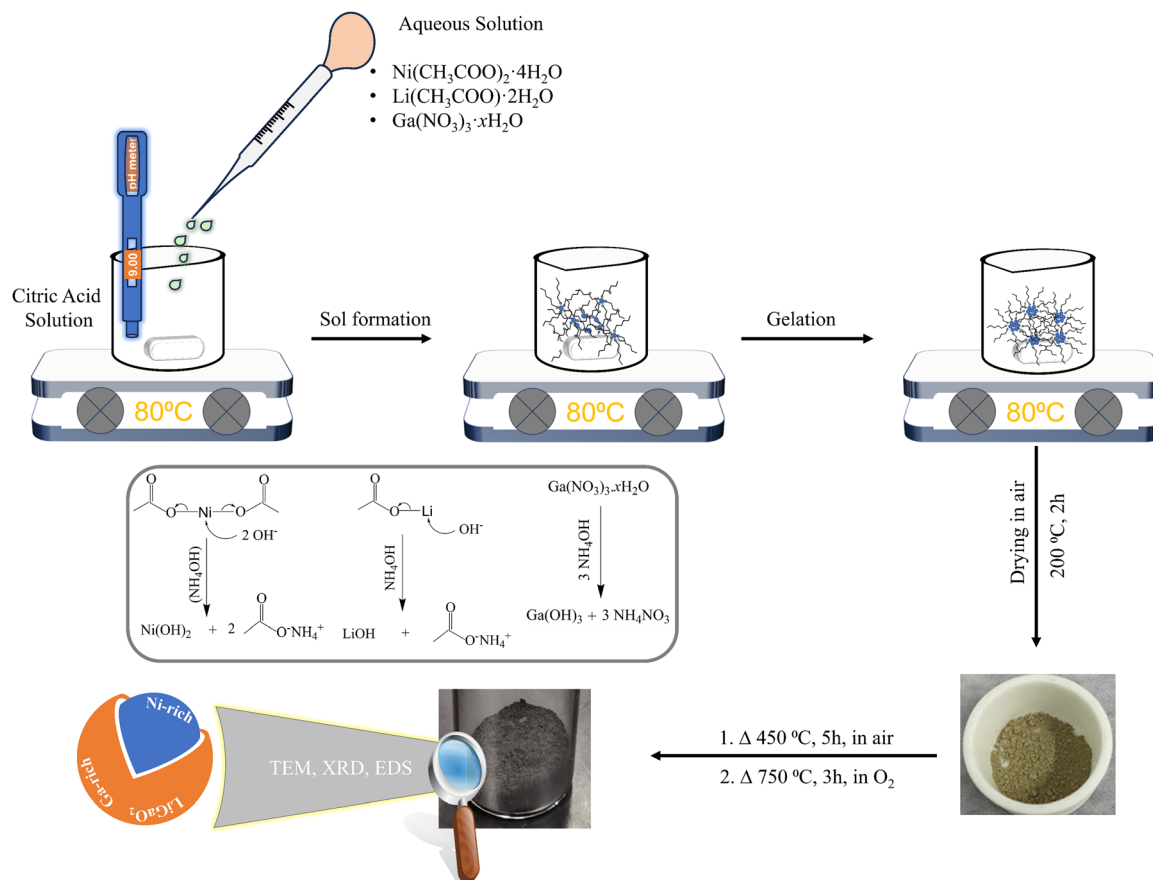
Scheme 1 Schematic of the synthesis route of 0–6% Ga–$LiNiO_2$ using a sol–gel method.

Table 1 Quantities of metal salts and chelating reagent (in grams) added during the synthesis of 0% to 6% Ga–LiNiO$_2$

Compound	Li(CH$_3$COO)·2H$_2$O	Ni(CH$_3$COO)$_2$·4H$_2$O	Ga(NO$_3$)$_3$·xH$_2$O	Citric acid
0% Ga–LiNiO$_2$	1.101	2.480	—	1.000
1% Ga–LiNiO$_2$	1.101	2.455	0.026	1.000
2% Ga–LiNiO$_2$	1.101	2.438	0.050	1.000
4% Ga–LiNiO$_2$	1.101	2.438	0.101	1.000
5% Ga–LiNiO$_2$	1.101	2.438	0.135	1.000
6% Ga–LiNiO$_2$	1.101	2.438	0.153	1.000

molar concentrations (0% to 6%), aqueous solutions of Li(CH$_3$COO)·2H$_2$O, Ni(CH$_3$COO)$_2$·4H$_2$O, and Ga(NO$_3$)$_3$·xH$_2$O were prepared in a 50 mL volume of deionized water. Concurrently, a chelating agent solution was prepared by dissolving 1 g of citric acid in 100 mL of deionized water. The solution pH was maintained at 9 through the addition of NH$_4$OH. The specific quantities of the aforementioned metal salts and citric acid employed in the synthesis are itemized in Table 1. The aqueous metal salts solution was introduced dropwise into the citric acid solution under constant stirring followed by heating at a temperature of 80 °C to produce the gel. The gel was subsequently dried at 200 °C for 2 h, producing the precursor powder. The precursor underwent a 450 °C treatment for 5 h in open atmosphere to eliminate carbonaceous impurities. Finally, the powder was annealed at 750 °C in a tube furnace under high-purity oxygen (99.997% O$_2$, Keen Gas grade 4.7) for 3 h to obtain the final cathode material. The heating and subsequent cooling rates were 5 °C min^{-1}.

Material characterization

X-ray diffraction (XRD) patterns were obtained using a Bruker D8 Discover (λ_{Cu} = 1.5406 Å) diffractometer in Bragg–Brentano mode. Patterns were collected from 10° to 80° 2θ for the as-synthesized as well as cycled 0%, 2% and 5% Ga–LiNiO$_2$ electrodes. Scanning electron microscopy (SEM) and energy-dispersive X-ray spectroscopy (EDS) were performed using a JEOL JSM-7400F at 3 kV and 15 kV, respectively. High resolution transmission electron microscopy (HRTEM, JEOL JEM-2010F) was obtained for pristine 0% and 5% Ga–LiNiO$_2$ at 200 kV. Prior to imaging, the powders were dispersed in isopropyl alcohol (IPA) under sonication and drop-cast onto TEM grids. X-ray photoelectron spectra (XPS) of 0%, 2%, and 5% Ga–LiNiO$_2$ cathodes were carried out using a Thermo Scientific K-Alpha XPS spectrometer (Al Kα source, spot size = 400 μm).

Electrode fabrication, battery assembly, and galvanostatic cycling

To produce 0–6% Ga–LiNiO$_2$ electrodes for electrochemical testing, slurries were prepared by mixing 80% active material, 10% super P carbon, and 10% PVDF (polyvinylidene difluoride) in N-methyl-2-pyrrolidone (NMP) using a planetary centrifugal mixer (Thinky AR-100). The resulting slurry was coated onto an aluminum foil using a doctor-blade with the wet coating thickness set to 200 μm. The coated electrodes were dried at 120 °C in a vacuum oven for 24 h followed by calendering to a thickness of ~50 μm resulting in a mass loading of ~4 mg cm^{-2}.

CR2032 coin cells were assembled in an argon-filled glovebox (<0.1 ppm O$_2$ and H$_2$O); 1 M LiPF$_6$ in ethylene carbonate/ethyl methyl carbonate (1 M LiPF$_6$ in EC : EMC = 1 : 1 v/v) procured from Millipore Sigma™ was used as the electrolyte. Lithium foil and LiNiO$_2$ electrodes were 14 mm in diameter and a 16 mm Celgard 2325 trilayer microporous separator was used. Half cells were constructed in the configuration LiNiO$_2$ (0–6% Ga) || 40 μL of 1 M LiPF$_6$ in EC : EMC = 1 : 1 v/v || Li foil. Galvanostatic charge–discharge (GCD, NEWARE battery cycler) measurements were performed at various C-rates (1C = 180 mA h g^{-1}) within the potential window of 3.0–4.3 V. Electrochemical impedance spectroscopy (EIS) was performed using a PARSTAT™ PMC-200 bipotentiostat with perturbation frequencies from 1 MHz to 0.01 Hz.

Results and discussion

Ga is doped from 0% to 6% into LiNiO$_2$ to understand the electrochemical performance of Ga doped LiNiO$_2$. EDS is used to empirically quantify the molar ratios of Ga to Ni in the doped particles. Fig. S1 (ESI†) provides details of the EDS data collected for the 1% to 6% Ga–LiNiO$_2$ powders. Performing spectroscopy at three randomly selected locations in the dispersed powder, some heterogeneity is observed in the levels of Ga from particle to particle. The average Ga/Ni molar ratios are slightly lower than the targeted values for all doping levels (Table S3, ESI†). Deviation from the targeted value is likely due to unquantified hydration on the Ga(NO$_3$)$_3$·xH$_2$O precursor during precursor weighing. 0–6% Ga–LiNiO$_2$ half-cells were cycled at C/3 for 100 cycles between 3.0 V and 4.3 V and their performance is presented in Fig. 2a. The summary of capacity retention in Fig. 2b shows scattered performance gains below 2% doping; 2% molar ratio of Ga is the reported solubility limit of Ga in LiNiO$_2$ at standard pressures.[14] The best performance below 2% doping is found at ~1% Ga; retention decreases again from 1 to 2% Ga. Most interestingly, Ga doping beyond its solubility limit of 2% results in a notable jump in the retention not attributable to potential cell to cell variations. Retention jumps from the 30% range to the >70% range and remains above this threshold from 4 to 6% The overall best capacity retention rate in the studied doping range of 0 to 6% is found at ~5% Ga doping with a retention of 76% at cycle 100 in a half-cell. Based on the retention trends in Fig. 2b, undoped LiNiO$_2$ (0% Ga), 2% Ga–LiNiO$_2$, and 5% Ga–LiNiO$_2$ were targeted to elucidate the electrochemistry and crystallography behaviors of undoped, solution-doped (at the solubility limit of 2%), and excess-doped LiNiO$_2$; the goal being to understand
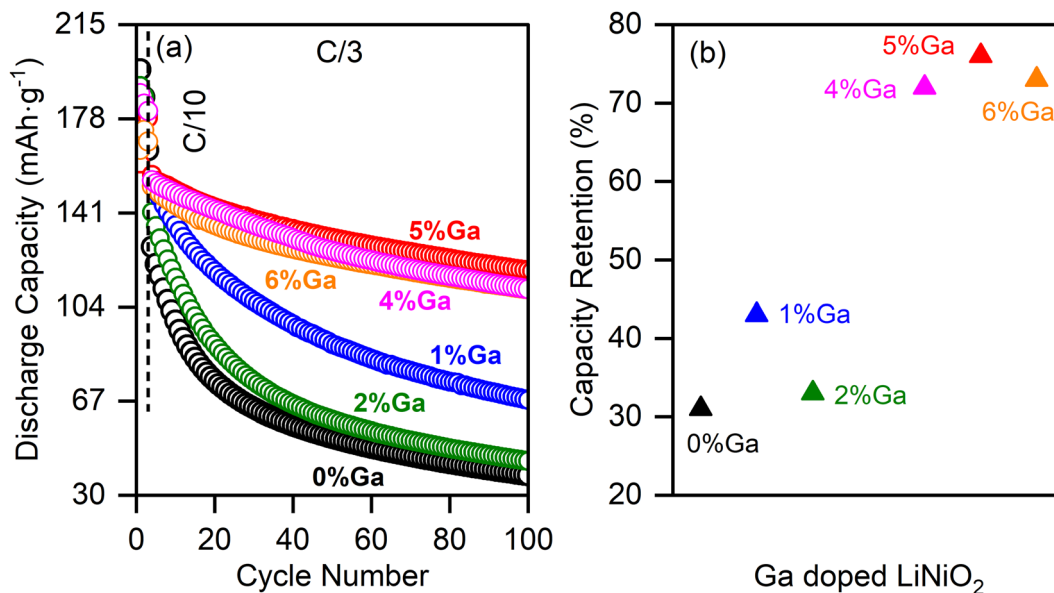
Fig. 2 Capacity retention during cycling of 0% to 6% Ga−LiNiO₂. (a) Discharge capacity *versus* cycle number at C/3; the first three formation cycles were obtained at C/10. (b) Capacity retention at cycle 100 of the various Ga doped LiNiO₂ summarized from (a); the best retention is found at ~5% Ga. Retention percentages are calculated as the ratio of discharge capacity at cycle 100 over the first C/3 capacity.
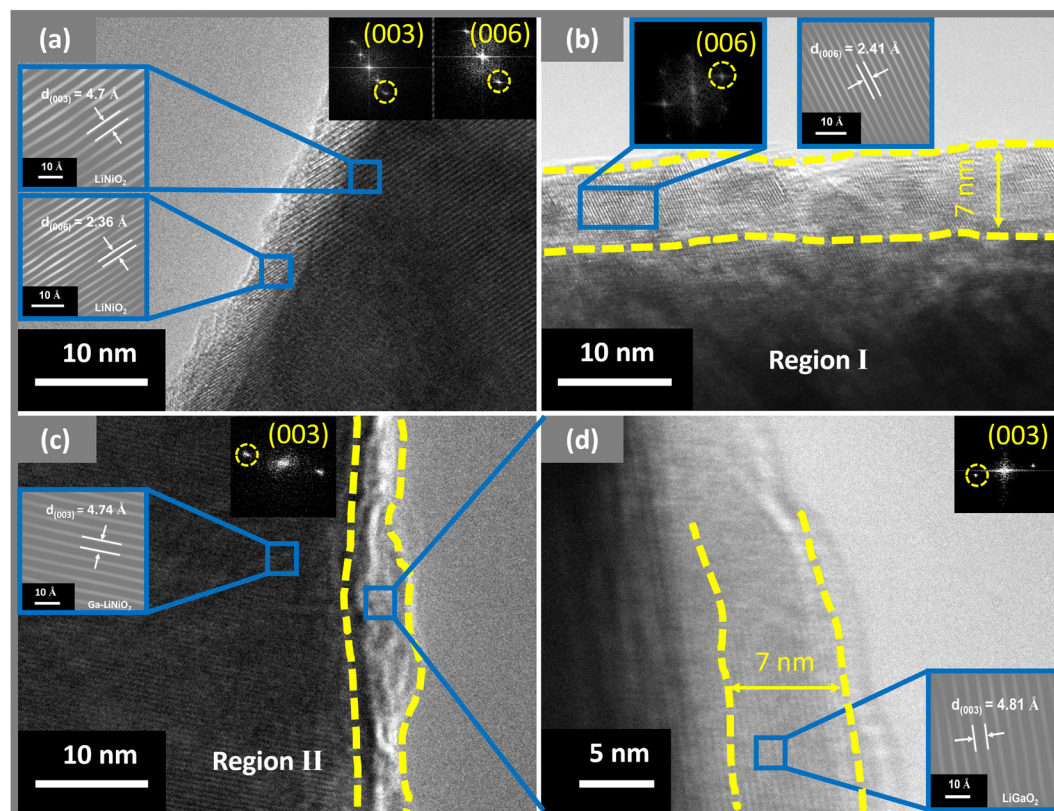

Fig. 3 HRTEM images of (a) 0% Ga−LiNiO₂, (b) 5% Ga−LiNiO₂ obtained in region I, (c) 5% Ga−LiNiO₂ obtained in region II, and (d) surface phase detected on 5% Ga−LiNiO₂. Corresponding FFT and IFFT images are shown in the inset.

the role or lack thereof of the Ga dopant surface segregation on cycling stability. Thereby, the bulk and surface crystallography of the as-synthesized material was investigated by HRTEM (Fig. 3). HRTEM of undoped LiNiO₂ shown in Fig. 3a reveals

d-spacings measuring 4.7 Å and 2.36 Å, which are readily assigned to the (003) and (006) Miller planes of $LiNiO_2$ in the $R\bar{3}m$ space group,[29] thereby confirming the intended phase. The 5% Ga–$LiNiO_2$ displays a slightly expanded core lattice with a (003) d-spacing of 4.74 Å (Fig. 3c); the larger Ga atom ($r(Ga^{3+})$ = 0.62 Å $vs.$ $r(Ni^{3+})$ = 0.56 Å) explains the c-expansion and corroborate a solution of Ga in the bulk of $LiNiO_2$.[14,30] However, the surface structure of the 5% Ga–$LiNiO_2$ differs significantly from its bulk; a thin shell ($\sim$7 nm) with larger plane spacings of 2.41 Å (Fig. 3b) and 4.81 Å (Fig. 3d) is resolved. Surprisingly, these measured lattice spacings match well with the reported parameters of the $R\bar{3}m$ isomorph of $LiGaO_2$ (α-$LiGaO_2$, lattice: $c \approx$ 14.466 Å),[28] whereby 4.81 Å and 2.41 Å match with the (003) and (006) plane spacings (14.466 Å/3 = 4.822 Å and 14.466 Å/6 = 2.411 Å). The presence of the $LiGaO_2$ surface phase on 5% Ga–$LiNiO_2$ is confirmed through the $Ga_2p_{3/2}$ XPS peak at 1117.13 eV, (Fig. S2e, ESI†). On the other hand, 2% Ga–$LiNiO_2$ (Fig. S2d, ESI†) shows extremely weak to non-existent Ga XPS signals indicating mostly bulk doping and no Ga-containing surface layer (note that the Ga signal from the bulk in 2% Ga–$LiNiO_2$ is resolved in EDS). HRTEM of 2% Ga–$LiNiO_2$ was not attempted as XPS and EDS line scan data discussed later below ruled out a shell phase. Ga doping reduces cation mixing favouring the anticipated Ni^{3+} as is evident by the increasing the Ni^{3+}/Ni^{2+} ratio in XPS with increasing Ga content (Table S4, ESI†).

The X-ray diffraction (XRD) spectra of all 0–6% Ga–$LiNiO_2$ are shown in Fig. S3 (ESI†). Detailed XRD analyses of the three targeted Ga–$LiNiO_2$ powders (0%, 2% and 5% Ga) are presented in Fig. 4a. The major peaks are all indexable to the intended α-$NaFeO_2$-type crystal for all three levels of doping. Well-segregated (006)/(012) and (110)/(108) reflections (Fig. 4b and c) confirm the layered structure of the produced oxides. The $I_{(003)}/I_{(104)}$ ratios in all three powders exceed 1.2 indicating negligible cation mixing. Rietveld refinements of 0%, 2%, and 5% Ga–$LiNiO_2$ result in satisfactory weighted profile reliability factors (R_{wp}) of 7.4%, 7.12% and 8.47%, respectively (Fig. 4d–f). The full-width at half-maximum (FWHM) of the (003) peaks (Table S5, ESI†) show significant broadening for 5% Ga–$LiNiO_2$ (21–33% greater than the 0 and 2% Ga–$LiNiO_2$ doping levels, see Fig. S4a, ESI†) pointing again to a potential secondary $R\bar{3}m$ phase. Aided by the HRTEM findings, a secondary phase of α-$LiGaO_2$ is introduced during the refinement of 5% Ga–$LiNiO_2$; refinement in the absence of this secondary phase yielded poor R_{wp}. An overall downshift of the (003) reflection is observed as the Ga content increases from 0% to 2% to 5% (Fig. S4a, ESI†) indicating an increase in the c-parameter from Ga-doping. Expansion of the c-parameter upon Ga doping is confirmed by the refinement (Table 2), which is supported by the HRTEM findings above. The c/a ratios are similar for the undoped $LiNiO_2$ and Ga-doped $LiNiO_2$ phases; the insertion of Ga in the $LiNiO_2$ lattice does not appear to significantly affect the extent of trigonal distortion within the materials. The detailed refinement results are provided in Tables S6, S7 and S8 (ESI†) for 0%, 2%, and 5% Ga–$LiNiO_2$, respectively. Occupancy refinement for the undoped $LiNiO_2$ ($i.e.$, 0% Ga) finds
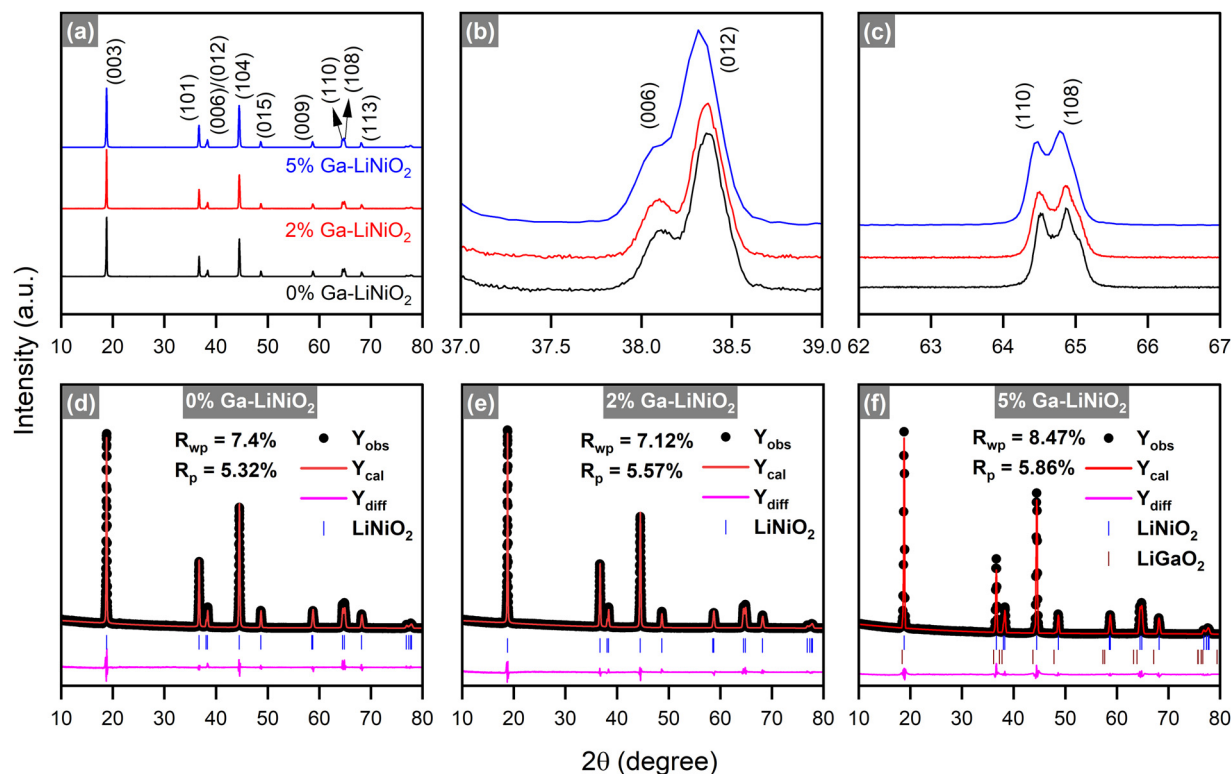

Fig. 4 (a)–(c) X-ray diffraction patterns and (d)–(f) Rietveld refined profiles of 0% Ga–$LiNiO_2$, 2% Ga–$LiNiO_2$, and 5% Ga–$LiNiO_2$. The 2θ axis is with respect to Cu Kα (λ = 1.5406 Å).

Table 2 Refined cell parameters and c/a ratio of synthesized LiNiO$_2$ and gallium doped LiNiO$_2$

	a (Å)	c (Å)	c/a
LiNiO$_2$	2.8770	14.2052	4.9375
2% Ga–LiNiO$_2$	2.8814	14.2293	4.9383
5% Ga–LiNiO$_2$			
Phase 1 (Ga-doped LiNiO$_2$)	2.8810	14.2263	4.9379
Phase 2 (LiGaO$_2$)	2.90648	14.4356	4.9667

∼3.6% Ni at the Li site (Wycoff 3a) reciprocated by ∼3.6% Li at the Ni site (Wycoff 3b). In the Ga-doped powders, Ga in the bulk is found to predominantly occupy the Li site with a minor presence at the Ni site for both 2% Ga–LiNiO$_2$ and 5% Ga–LiNiO$_2$. Notably, acceptable refinement ($R_{wp} < 10\%$) for the 5% Ga–LiNiO$_2$ did not necessitate increase in the Ga occupancy (*vs.* occupancy in 2% Ga–LiNiO$_2$) at the 3a and 3b sites. Specifically, a Ga occupancy of 1.6–1.7% at the Li 3a site was calculated after Rietveld convergence for both the 2% and 5% levels of doping. Furthermore, the change in the primary phase c-parameter between 2% and 5% Ga-doped (∼0.003 Å) is 6.7 times less than the ∼0.02 Å increase from 0% to 2% Ga-doped (Table 2). These observations confirm the reported bulk solubility limit near 2% Ga at standard pressure conditions.[14]

Kitsche *et al.*[14] reported the growth of secondary peaks corresponding to Li$_5$GaO$_4$ in the range $8.4 \leq 2\theta_{\lambda=0.62\text{Å}} \leq 13.3$ ($20.97 \leq 2\theta_{\lambda=1.5406\text{Å}} \leq 33.44$), which strengthened with the increasing Ga-content. Magnifying this region in our spectra (Fig. S4b, ESI†), no peaks corresponding to Li$_5$GaO$_4$ are resolved in our Ga doped powders. Instead, minor peaks attributed to Li$_2$CO$_3$, a common impurity on LiNiO$_2$, are resolved in both the undoped and Ga doped powder spectra. Furthermore, the surface phase observed by HRTEM displays a d-spacing of 4.81 Å; the nearest d-spacing in the Li$_5$GaO$_4$ crystal is ∼4.6 Å for the (002) planes excluding it as the likely phase. The referenced study utilized a chelating agent-free wet-mixing synthesis approach and annealing under O$_2$ was done at 700 °C. In contrast, our sol–gel synthesis makes use of citric acid as a chelating agent and the annealing is performed at 750 °C under O$_2$. It is understood that minor alterations in the synthesis approach can significantly impact the phase(s) in the final product.

HRTEM in Fig. 3b and c above suggests a shell phase on the 5% Ga–LiNiO$_2$ particle which, from the evidence discussed thus far, appears to be Ga rich (α-LiGaO$_2$). An EDS line scan is obtained for 2% and 5% Ga–LiNiO$_2$ with the goal of resolving such core–shell structure from the predictable signal patterns in such configuration. Modeling of the expected line scan signal pattern for a spherical core–shell configuration is provided in Fig. S5 (ESI†) with the corresponding pseudo-code of the simulation. In a core–shell configuration such as that shown schematically in Fig. 5a, the Ga signal would jump to a maximum at the edge ($x_1 \rightarrow x_2$) of the scan where the beam would graze mostly the Ga-rich shell and then decrease to local minimum where it would plateau onward ($x_2 \rightarrow x_3$). The Ni-rich core signal would increase to a maximum and remain at this
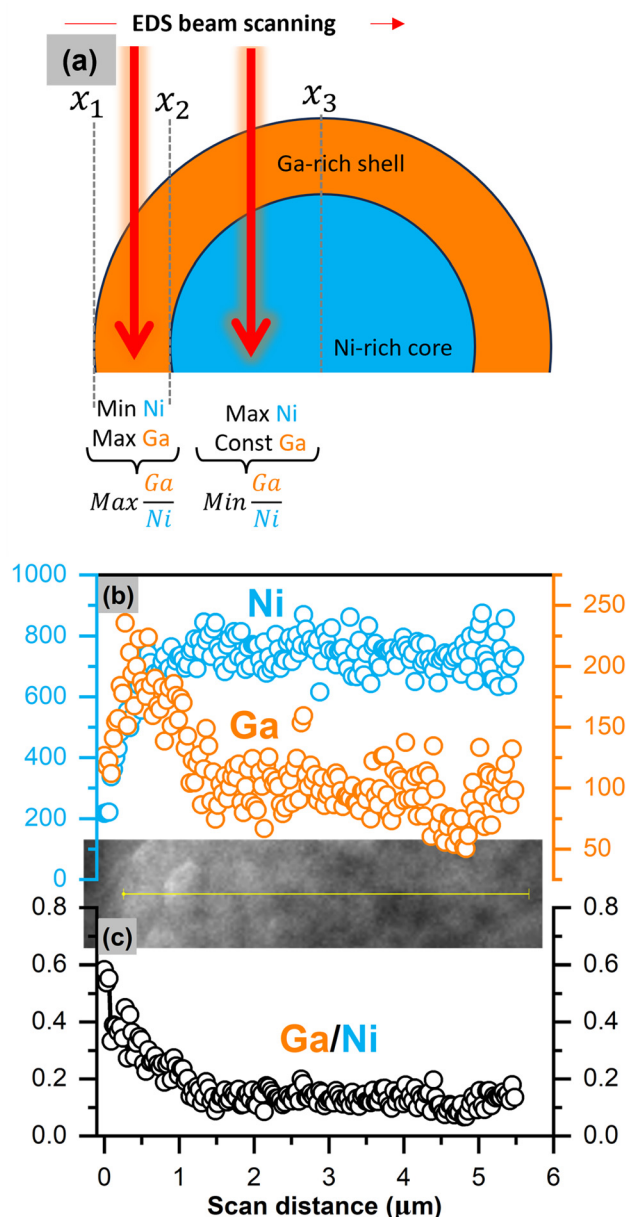
Fig. 5 (a) Schematic representation of core–shell model under the EDS line scan. (b) and (c) Ga and Ni EDS count and ratio *versus* EDS scan distance from particle's edge for 5% Ga–LiNiO$_2$. The image inset between (b) and (c) is the actual SEM image during the line scan.

maximum as the beam scans toward the particle center. This pattern is verified in the experimental data collected for 5% Ga–LiNiO$_2$ as shown in Fig. 5b whereby starting from the edge of the particle inward, the EDS signal of Ga jumps to a maximum before decreasing and plateauing to a constant value. Meanwhile, the Ni signal increases to a maximum value and maintains this maximum value as the beam moves towards the particle center. Both signals track well with the core–shell EDS simulation (see Fig. S5a, ESI†). The Ga/Ni ratio calculated over a line scan (Fig. 5c) is highest at the edge of the scan, rapidly decreases before plateauing, again tracking the simulation trend in Fig. S5b (ESI†). In contrast, for the 2% Ga–LiNiO$_2$

(anticipated as a solid-solution), the Ga and Ni signals both jump to their maxima whence the EDS beam reaches the particle (Fig. S6, ESI†). Unlike the 5% Ga–LiNiO$_2$, the Ga signal in the 2% Ga–LiNiO$_2$ does not decrease meaningfully before plateauing. Instead, the Ni and Ga signals fluctuate about the maxima during the spatial scan indicating a homogenous solution. Thereby, we confirm a Ga-rich shell on 5% Ga–LiNiO$_2$ which we assign to α-LiGaO$_2$ based on HRTEM, XRD, and XPS discussed above while at 2% Ga no Ga-rich shell is detected but instead a solid-solution.

The galvanostatic charge–discharge profiles of undoped and Ga–LiNiO$_2$ are shown in Fig. 6a–c. The 0%, 2%, and 5% Ga-doped LiNiO$_2$ achieved initial C/10 discharge capacities of 197 mA h g^{-1}, 192 mA h g^{-1}, and 174 mA h g^{-1}, respectively. On the one hand, the systematic reduction in the extracted specific capacity as the Ga content increases is partly due to the increasing proportion of inactive Ga phases; the calculated theoretical specific capacities in Table S9 (ESI†) support this trend. On the other hand, the measured loss of ∼20 mA h g^{-1} after 5% Ga doping is disproportionate *versus* the expected ∼6 mA h g^{-1} loss from the doping especially at such low C/10 rate; the LiGaO$_2$ surface phase could be impeding the Li$^+$ exchange at the surface.

Indeed, a higher charge transfer resistance (R_{ct}) is found for 5% Ga–LiNiO$_2$ electrodes (R_{ct} ∼ 130 Ω) compared to the 0% (R_{ct} ∼ 105 Ω) and 2% (R_{ct} ∼ 100 Ω) Ga–LiNiO$_2$ electrodes (Fig. S7a, ESI†). Decreased kinetics is therefore the likely source of the ∼20 mA h g^{-1} decrease in capacity between undoped and 5% doped Ga–LiNiO$_2$ at C/10.

The evolution of distinct phases is probed *via* the differential capacity (dQ/dV); the 3rd cycle is used for this purpose in order to analyze the stabilized state of the cell (Fig. 6d). The typical dQ/dV peaks revealing five distinct phases (H$_1$, H$_1'$, M, H$_2$ and H$_3$) of LiNiO$_2$ are present in the undoped and Ga-doped cathodes.[7,31,32] The dQ/dV peak intensities of H$_1'$ ↔ M, M ↔ H$_2$, and H$_2$ ↔ H$_3$ interconversions generally become lower and broader as the Ga content increases. However, the H$_2$ ↔ H$_3$ peaks of the 5% Ga–LiNiO$_2$, both on oxidation and reduction, are most significantly depressed and shifted rightward (to higher voltages) compared to both 0% and 2% Ga–LiNiO$_2$; the right-shift is consistent on the first and second cycles (Fig. S8, ESI†). Although some shift in the H$_1'$ ↔ M and M ↔ H$_2$ as Ga content increases can be noted, they are subdued compared to the displacement of the H$_2$ ↔ H$_3$ in 5% Ga–LiNiO$_2$. Biasi *et al.*[7] concluded using DEMS that O$_2$ loss in LiNiO$_2$ is most vigorous during the solid-solution delithiation of the H$_2$ and later H$_3$ phases. Nonetheless, the intensity of H$_2$ → H$_3$ peak correlates with the O$_2$ loss; DEMS by Park *et al.*[8] found O$_2$ loss on uncoated-LiNiO$_2$ spanning the entire H$_2$ to H$_3$ phase range while minimal loss from graphene-coated LiNiO$_2$ coincides with a depressed H$_2$ → H$_3$ peak. Thereby, the upshift (+20 mV) and magnitude reduction of the anodic H$_2$ → H$_3$ conversion as Ga increases herein signal reduction in detrimental O$_2$ loss likely afforded by the surface α-LiGaO$_2$ on the 5% Ga–LiNiO$_2$. It is notable that the H$_2$ → H$_3$ peak of the 2% Ga–LiNiO$_2$ does not differ as significantly in position and magnitude from the undoped LiNiO$_2$ (contrary to the 5% Ga–LiNiO$_2$, Fig. 6d). Specific capacities of 38 mA h g^{-1}, 45 mA h g^{-1}, and 118 mA h g^{-1} are recorded at the 100th C/3 cycle for 0%, 2%, and 5% Ga–LiNiO$_2$, respectively (Fig. 2a). In keeping with its depressed and upshifted anodic H$_2$ → H$_3$ peak signaling a lower rate of O$_2$ loss, the 5% Ga–LiNiO$_2$ retains distinctly higher capacity at C/3 (76%) after 100 cycles compared to 2% Ga–LiNiO$_2$ (33%) and 0% Ga–LiNiO$_2$ (31%).

The coulombic efficiencies (CE) during cycling are shown in Fig. S9 (ESI†). The first cycle CE are 89.3% 89.7%, and 82% for 0, 2, and 5% Ga, respectively. The lower initial CE of 5% Ga–LiNiO$_2$ is tentatively ascribed to the presence of LiGaO$_2$ surface coating causing higher impedance in the early cycles (Fig. S7a, ESI†). Following three formation cycles, the CE of the 0% and 2% Ga–LiNiO$_2$ progressively increases, crossing 99% at cycle 25. The 5% Ga–LiNiO$_2$ on the other hand achieved a CE of ∼99.6% immediately after three formation cycles and maintained this CE for the remaining 100 cycles. The more stable CE of 5% Ga–LiNiO$_2$ aligns with indications of reduced O$_2$ loss and may further reflect the absence of particle pulverization and accompanying more stable CEI compared to the 0 and 2% Ga–LiNiO$_2$ (discussed below).

Postmortem XRD analysis of the electrodes after the 100th lithiation cycle shows substantial downshift in the 2$\theta_{(003)}$ value for 0% and 2% Ga-doped LiNiO$_2$ (Fig. 7a) compared to the as-synthesized state. This downshift suggests the post-cycling Li content in those cathode materials is significantly lower (expanded c-axis) compared to the as-synthesized powder. The 2$\theta_{(003)}$ of 5% Ga-doped LiNiO$_2$ experiences approximately half the 2$\theta_{(003)}$ downshift of 0% and 2% Ga-doped LiNiO$_2$ after 100 cycles, indicating less Li$^+$ loss in agreement with its increased capacity retention in Fig. 2a.

One of the defining modes of failure of LiNiO$_2$ cathode particles is cracking and pulverization during extended cycling.[8] Therefore, pre-, and post-cycling SEM images of particles in the electrodes are presented in Fig. 7b–g. The starting active material for all three levels of doping are spheroidal aggregates of nano-sized primary particles into secondary particles on the order of 10–20 μm. The undoped 0% (Fig. 7b *vs.* Fig. 7e) and solution-doped 2% (Fig. 7c *vs.* Fig. 7f) Ga–LiNiO$_2$ particles experience extensive pulverization after 100 C/3 cycles. The starting aggregates are shattered into their primary particles in Fig. 7e and f. In contrast, the 5% Ga–LiNiO$_2$ shows far fewer shattered aggregates after 100 cycles (Fig. 7d *vs.* Fig. 7g). Multiple locations on the electrode surfaces were surveyed to ensure the statistical validity of these observations (see Fig. S10–S12, ESI†). Shattering of the secondary particle such as seen for the 0% and 2% Ga–LiNiO$_2$ produces smaller particles increasing the surface area exposed to the electrolyte. In turn the large area increases parasitic reactions at the cathode∥electrolyte interface that consume Li$^+$ from active cathode.[29,33,34]

HRTEM images were acquired for 0%, 2%, and 5% Ga–LiNiO$_2$ samples after 100 cycles to investigate the cathode surface. In Fig. 7h and i, both the 0% and 2% Ga-doped LiNiO$_2$ particles have a thick amorphous (no diffraction spots in the FFT) interphase layer on the surfaces. Conversely, no such amorphous
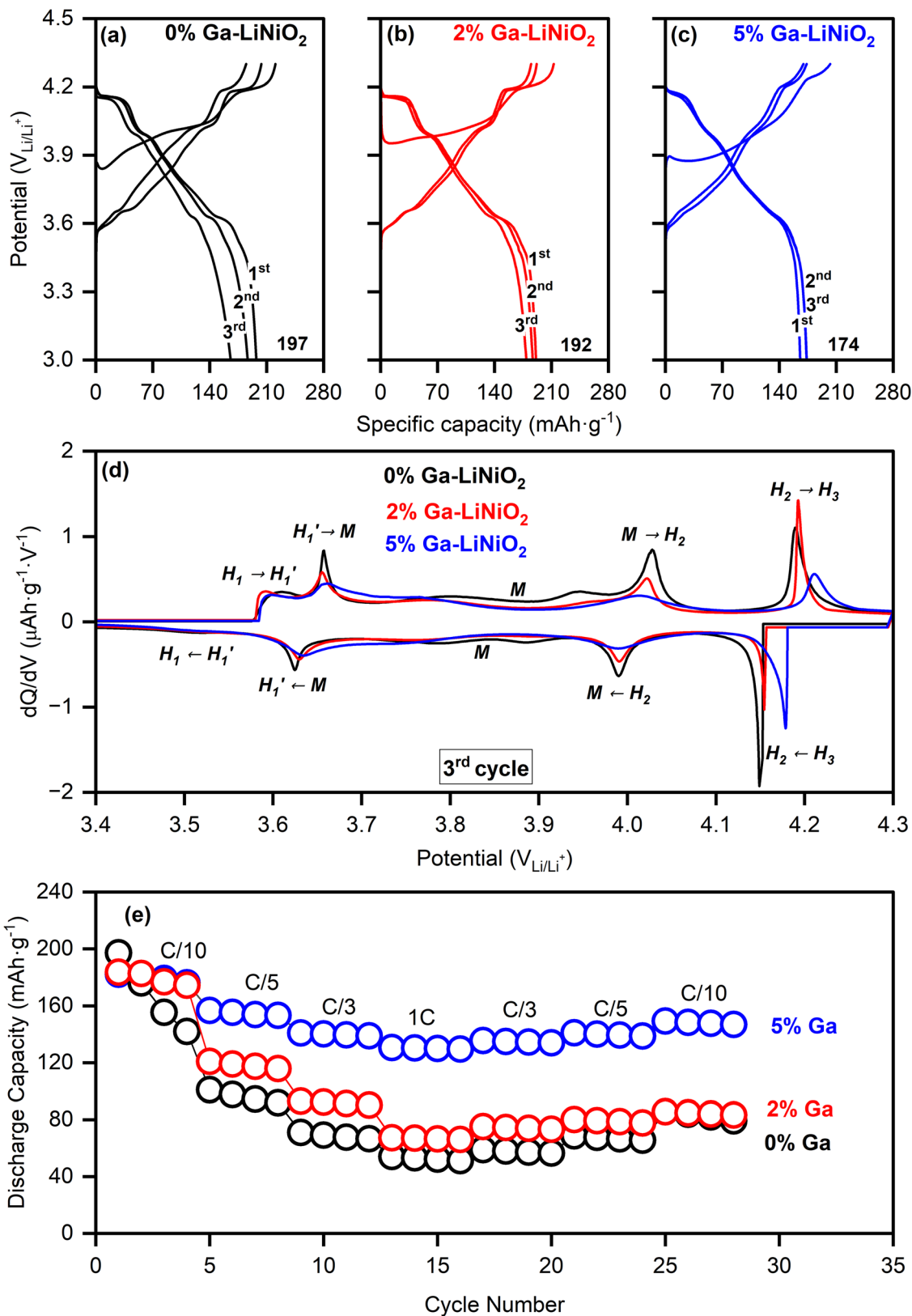
Fig. 6 Galvanostatic charge–discharge at C/10 (1C = 180 mA g^{-1}) of (a) 0% Ga–LiNiO$_2$, (b) 2% Ga–LiNiO$_2$, (c) 5% Ga–LiNiO$_2$. (d) Differential capacities (dQ/dV) *versus* voltage of the same. (e) Rate capability performance of 0%, 2%, and 5% Ga–LiNiO$_2$.
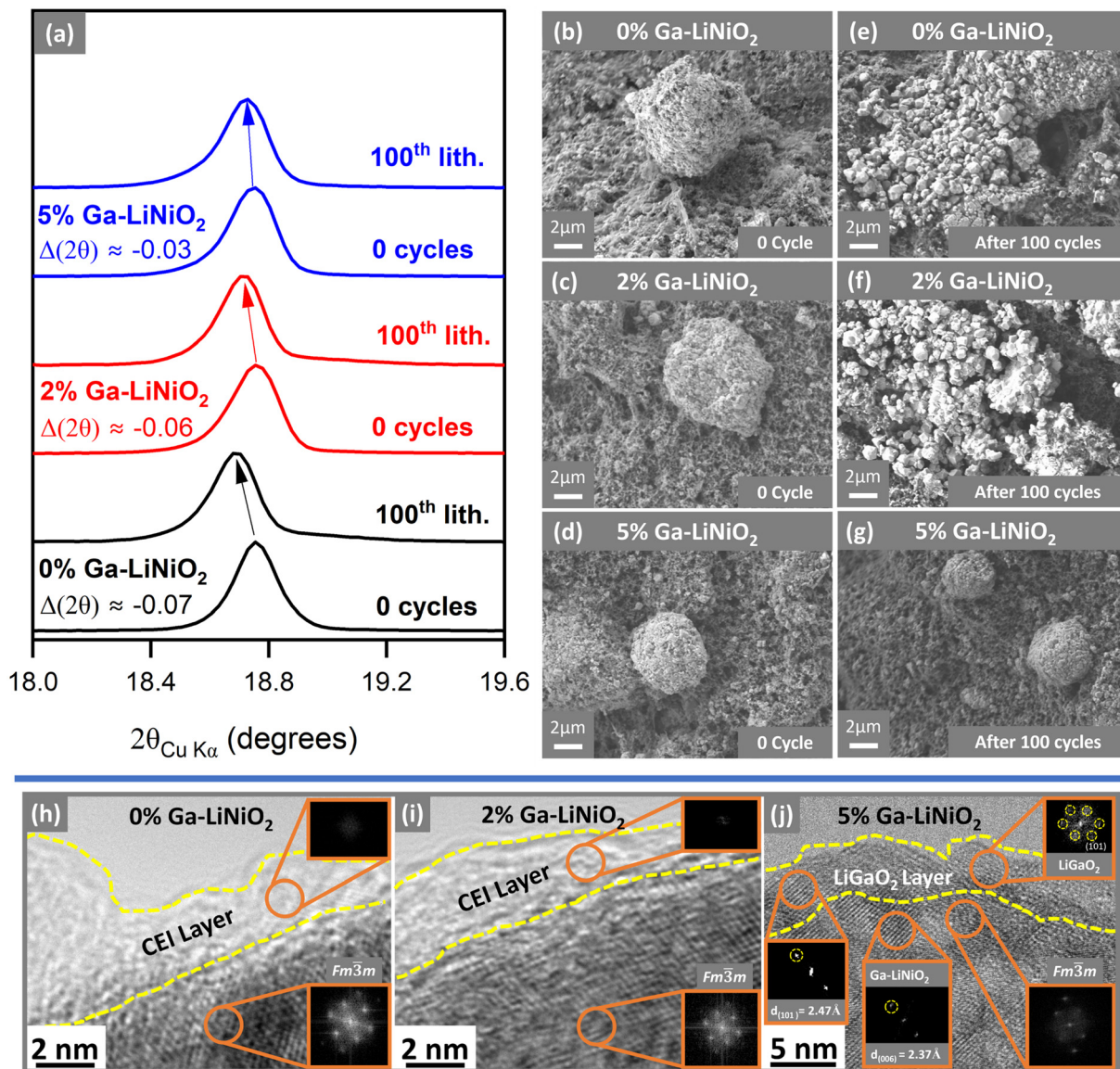
Fig. 7 (a) (003) XRD reflections of pristine *vs.* 100th lithiation cycle of 0%, 2%, and 5% Ga–LiNiO$_2$ half-cells SEM images of Pristine electrodes (b)–(d) and electrodes after 100 cycles (e)–(g) of 0% Ga–LiNiO$_2$, 2% Ga–LiNiO$_2$ and 5% Ga–LiNiO$_2$ cathodes. (h)–(j) HRTEM images of 0%, 2%, and 5% Ga–LiNiO$_2$ after 100 cycles.

phase is resolved on the surface of 5% Ga-doped LiNiO$_2$ sample (Fig. 7j). The presence of a LiGaO$_2$ surface layer on 5% Ga-doped appears to diminish the parasitic CEI reactions partly responsible for irreversible Li$^+$ loss from the lattice. The surface LiGaO$_2$ on 5% Ga–LiNiO$_2$ has a more significant impact on increasing capacity retention compared to only bulk doping in 2% Ga–LiNiO$_2$. The preservation of the surface α-LiGaO$_2$ phase on 5% Ga–LiNiO$_2$, post 100 cycles, is confirmed *via* the *d*-spacing of 2.47 Å corresponding to its (101) miller planes (Fig. 7j). In contrast, no such *d*-spacing is found on the surface of 2% Ga–LiNiO$_2$ post 100 cycles (Fig. 7i); a confirmation that no surface gallate layer was formed at synthesis.

The absence of the surface gallate on 2% Ga–LiNiO$_2$ coincides with extensive near surface reconstruction to rocksalts in the *Fm$\bar{3}$m* space group; the surface of 0% Ga–LiNiO$_2$ is similarly

reconstructed. In contrast, with α-LiGaO$_2$ remaining on the surface of 5% Ga–LiNiO$_2$, the $d_{(006)}$ = 2.37 Å corresponding the *R$\bar{3}$m* layered LiNiO$_2$ is still detectable in the near surface region (Fig. 7j). A few *Fm$\bar{3}$m* rocksalt spots are detected however, suggesting some, although markedly reduced surface reconstruction (Fig. S13, ESI†).

The rapid capacity fade of the 0% and 2% Ga–LiNiO$_2$ are easily attributable to their pulverization and surface changes. This claim is supported by the EIS of cycled electrodes. The impedance growth after 100 C/3 cycles is nearly fourfold lower for the 5% Ga compared to the 0% and 2% Ga–LiNiO$_2$ (Fig. S7b, ESI†), a reflection of the drastically diminished particle breakage and thereby lower exposed surface area for reconstruction and resistive CEI growth. Particle shattering has been linked to O$_2$ loss and mechanical fatigue from repeated phase

transitions.[8] The surface α-LiGaO$_2$ observed by HRTEM and the accompanying depressed H$_2$ → H$_3$ transitions in 5% Ga–LiNiO$_2$ supports mitigation of these factors which explains the preservation of the integrity of secondary particles over 100 cycles.

Given the greater capacity retention at C/3, the rate capability of 5% Ga–LiNiO$_2$ was compared against the 2% and baseline 0% Ga–LiNiO$_2$ at C/10, C/5, C/3, and 1C rate (Fig. 6e). As expected, the capacity output of three cathodes decreases with increasing C-rate due to polarization; however, the performance of 5% Ga–LiNiO$_2$ significantly exceeds that of the baseline and 2% Ga–LiNiO$_2$ in agreement with the C/3 result in Fig. 2a. At 1C, 5% Ga–LiNiO$_2$ achieves $\sim$130 mA h g^{-1} while 2% and 0% Ga–LiNiO$_2$ only achieve $\sim$67 and $\sim$52 mA h g^{-1} respectively. The intercalation kinetics appear more efficient in the presence of the surface gallate layer which matches with the suppressed growth of the charge transfer resistance shown in Fig. S7b (ESI†). As the 5% Ga–LiNiO$_2$ particles do not crack to expose more surface area, the growth of kinetically unfavorable cathode electrolyte interphase (CEI) is curtailed by the surface LiGaO$_2$ to maintain optimal intercalation kinetics.

Conclusions

Cobalt-free, Ga-doped LiNiO$_2$ were produced with 0%, 1%, 2% (solution-doped), and 4%, 5%, 6% (excess-doped) Ga to Ni molar ratios with the goal of resolving the role of surface gallium–oxide phases. Under the sol–gel synthesis method utilized, XRD, HRTEM, and EDS show the unusual formation of an α-LiGaO$_2$ surface layer on LiNiO$_2$ when the Ga molar ratio exceeds its reported solubility in LiNiO$_2$ in the excess-doped particles. Comparing the electrochemistries of solution-doped and excess-doped Ga–LiNiO$_2$, the α-LiGaO$_2$ coating appears key to softening the high-voltage H$_2$ → H$_3$ phase transformation, which correlates with the drastically reduced O$_2$ loss, surface reconstruction, and fracturing in the cathode material. Further validation using SEM imaging post 100 cycles shows markedly reduced particle cracking only in the excess-doped 5% Ga–LiNiO$_2$ particles; the undoped and solution-doped LiNiO$_2$ particles display extensive fracturing. Post-mortem HRTEM uncovers suppressed surface reconstruction of the particle only in the presence of the α-LiGaO$_2$ surface layer on 5% Ga–LiNiO$_2$. The result of the suppression of these damaging processes is significantly enhanced capacity retention and rate capability. A retention rate of 76% in half-cells is observed for 5% Ga–LiNiO$_2$ compared to 31% and 33% for similarly synthesized undoped and solution-doped LiNiO$_2$. This finding underscores the role and necessity of the surface gallium oxide phase in suppressing the processes responsible for O$_2$ loss, surface reconstruction, particle pulverization, and Li$^+$ loss in LiNiO$_2$.

Author contributions

MM collected the research data and prepared the manuscript figures and drafting. KPCY is the research P. I. and provided the research motivation, experimental planning, and manuscript editing.

Data availability

Conflicts of interest

There are no conflicts to declare.

Acknowledgements

References

1 M. M. Thackeray and K. Amine, *Nat. Energy*, 2021, **6**, 566.
2 M. Mishra, G. S. Taiwo and K. P. C. Yao, *ACS Appl. Mater. Interfaces*, 2022, **15**, 14261–14273.
3 T. Ohzuku, A. Ueda and M. Nagayama, *J. Electrochem. Soc.*, 1993, **140**, 1862–1870.
4 J. Cheng, B. Ouyang and K. A. Persson, *ACS Energy Lett.*, 2023, **8**, 2401–2407.
5 M. Bianchini, M. Roca-Ayats, P. Hartmann, T. Brezesinski and J. Janek, *Angew. Chem., Int. Ed.*, 2019, **58**, 10434–10458.
6 C. S. Yoon, D. W. Jun, S. T. Myung and Y. K. Sun, *ACS Energy Lett.*, 2017, **2**, 1150–1155.
7 L. de Biasi, A. Schiele, M. Roca-Ayats, G. Garcia, T. Brezesinski, P. Hartmann and J. Janek, *ChemSusChem*, 2019, **12**, 2240–2250.
8 K. Y. Park, Y. Zhu, C. G. Torres-Castanedo, H. J. Jung, N. S. Luu, O. Kahvecioglu, Y. Yoo, J. W. T. Seo, J. R. Downing, H. D. Lim, M. J. Bedzyk, C. Wolverton and M. C. Hersam, *Adv. Mater.*, 2022, **34**, 2106402.
9 J. Hu, L. Li, Y. Bi, J. Tao, J. Lochala, D. Liu, B. Wu, X. Cao, S. Chae, C. Wang and J. Xiao, *Energy Storage Mater.*, 2022, **47**, 195–202.

10 C. Wang, L. Han, R. Zhang, H. Cheng, L. Mu, K. Kisslinger, P. Zou, Y. Ren, P. Cao, F. Lin and H. L. Xin, *Matter*, 2021, **4**, 2013–2026.

11 J. Cheng, L. Mu, C. Wang, Z. Yang, H. L. Xin, F. Lin and K. A. Persson, *J. Mater. Chem. A*, 2020, **8**, 23293–23303.

12 C. S. Yoon, M. J. Choi, D. W. Jun, Q. Zhang, P. Kaghazchi, K. H. Kim and Y. K. Sun, *Chem. Mater.*, 2018, **30**, 1808–1814.

13 L. Wu, X. Tang, X. Chen, Z. Rong, W. Dang, Y. Wang, X. Li, L. Huang and Y. Zhang, *J. Power Sources*, 2020, **445**, 227337.

14 D. Kitsche, S. Schweidler, A. Mazilkin, H. Geßwein, F. Fauth, E. Suard, P. Hartmann, T. Brezesinski, J. Janek and M. Bianchini, *Mater. Adv.*, 2020, **1**, 639–647.

15 X.-Z. Kong, D.-L. Li, K. Lahtinen, T. Kallio and X.-Q. Ren, *J. Electrochem. Soc.*, 2020, **167**, 140545.

16 H. R. Park, *J. Ind. Eng. Chem.*, 2010, **16**, 698–702.

17 Y. Nishida, K. Nakane and T. Satoh, *J. Power Sources*, 1997, **68**, 561–564.

18 G.-X. Huang, R.-H. Wang, X.-Y. Lv, J. Su, Y.-F. Long, Z.-Z. Qin and Y.-X. Wen, *J. Electrochem. Soc.*, 2022, **169**, 040533.

19 H. U. Kim, J. Song, D. R. Mumm and M. Y. Song, *Ceram. Int.*, 2011, **37**, 779–782.

20 W. M. Seong and A. Manthiram, *ACS Appl. Mater. Interfaces*, 2020, **12**, 43653–43664.

21 J. Li, Y. Zhu, B. Pang and P. Gao, *J. Mater. Sci.*, 2022, **57**, 17722–17734.

22 M. Y. Song, S. N. Kwon and H. R. Park, *Ceram. Int.*, 2009, **35**, 3135–3141.

23 A. Mesnier and A. Manthiram, *ACS Appl. Mater. Interfaces*, 2020, **12**, 52826–52835.

24 C. S. Yoon, U. H. Kim, G. T. Park, S. J. Kim, K. H. Kim, J. Kim and Y. K. Sun, *ACS Energy Lett.*, 2018, **3**, 1634–1639.

25 H. Cao, F. Du, J. Adkins, Q. Zhou, H. Dai, P. Sun, D. Hu and J. Zheng, *Ceram. Int.*, 2020, **46**, 20050–20060.

26 S. H. Park, K. S. Park, Y. Kook Sun, K. S. Nahm, Y. S. Lee and M. Yoshio, *Electrochim. Acta*, 2001, **46**, 1215–1222.

27 S. L. Dreyer, P. Kurzhals, S. B. Seiffert, P. Müller, A. Kondrakov, T. Brezesinski and J. Janek, *J. Electrochem. Soc.*, 2023, **170**, 060530.

28 M. Marjzio and J. P. Remeika, *J. Phys. Chem. Solids*, 1965, **26**, 1277–1280.

29 H. Kaneda, Y. Furuichi, A. Ikezawa and H. Arai, *ACS Appl. Mater. Interfaces*, 2022, **14**, 52766–52778.

30 R. Stoyanova, E. Zhecheva, R. Alcántara, J. L. Tirado, G. Bromiley, F. Bromiley and T. B. Ballaran, *J. Mater. Chem.*, 2004, **14**, 366–373.

31 J. P. Peres, F. Weill and C. Delmas, *Solid State Ion.*, 1999, **116**, 19–27.

32 J. Chen, H. Yang, T. Li, C. Liu, H. Tong, J. Chen, Z. Liu, L. Xia, Z. Chen, J. Duan and L. Li, *Front. Chem.*, 2019, **7**, 00500.

33 T. Liu, L. Yu, J. Lu, T. Zhou, X. Huang, Z. Cai, A. Dai, J. Gim, Y. Ren, X. Xiao, M. V. Holt, Y. S. Chu, I. Arslan, J. Wen and K. Amine, *Nat. Commun.*, 2021, **12**, 6024.

34 R. Ruess, S. Schweidler, H. Hemmelmann, G. Conforto, A. Bielefeld, D. A. Weber, J. Sann, M. T. Elm and J. Janek, *J. Electrochem. Soc.*, 2020, **167**, 100532.